EAI Endorsed Transactions
on Mobile Communications and Applications
Research Article EAI.EU

Collaborative Relay Radio Network Using Reconfigurable Intelligent Surface

Huu Q. Tran[1,*] , Nguyen Trong Duy[1], Huynh Phan Hieu Nghia[1]

[1]Faculty of Electronics Technology (FET), Industrial University of Ho Chi Minh City (IUH)
(e-mail: tranquyhuu@iuh.edu.vn, nguyentrongduyc9@gmail.com, huynhphanhieunghia@gmail.com)

Abstract

In this paper, we have studied a model of a relay radio network system using Reconfigurable Intelligent Surface (RIS). Specifically, we used a relay network that uses RIS when there is an extra direct link from the Source (S) to the Destination (D). Next, an approximate closed-form expressions of the Outage Probability (OP) and Ergodic Capacity (EC) are considered. Based on the simulation results of OP and EC, the results show that our proposed system is more optimal than the system using supported RIS without direct link and the system without using RIS. In addition, changing the number of the RIS reflecting elements and the RIS's location near (S) or (D) has a significant impact on the performance of the system. The analytical expression match the simulation results through the Monte Carlo simulation method. Furthermore, the simulation results of energy efficiency (EE) also show that when the target spectral efficiency (SE), Rth, is high (more than 5.45 b/s/Hz), the system using supported RIS with direct link will help reduce the transmit power and optimize the most energy compared to the other two systems.

Keywords: RIS, OP, EC, Nakagami-m, Gamma.

Received on 01 June 2022, accepted on 13 September 2022, published on 21 September 2022

Copyright © 2022 Huu Q. Tran *et al.*, licensed to EAI. This is an open access article distributed under the terms of the CC BY-NC-SA 4.0, which permits copying, redistributing, remixing, transformation, and building upon the material in any medium so long as the original work is properly cited.

doi: 10.4108/eetmca.v7i3.2716

1. Introduction

5G network technology is the 5th network technology, the successor to the extremely popular 4G LTE connection before. As its successor, the 5G network enables the transmission of large amounts of data at outstandingly high speeds, improved bandwidth, reliability in connection, along with maintained signal latency. maintained to a minimum, … This will bring more challenging engineering problems, requiring new and more efficient communication models, especially at the physical layer.

To meet the diverse requirements of current 5G networks as well as for future B5G and 6G system design, Non-Orthogonal Multiple Access (NOMA) is identified as an important technology that can satisfy requirements mentioned above [1]. The most prominent feature of the NOMA technique is that it supports a larger number of USERs than the number of orthogonal resource slots through non-orthogonal resource allocation. Furthermore, NOMA's ease of integration with many technologies is also a strength, such as collaborative communication [2], Time Division Multiple Access (TDMA) [3], physical layer security [4], …The integration of NOMA with other physical layer techniques has been widely discussed based on different application scenarios and requirements in [5, 6] The collaborative NOMA communication concept proposed in [7], in which users with better conditions are selected as relays to ensure the service quality of edge users. Furthermore, the authors of [8, 9] investigated the full/half-duplex (FD/HD) performance of cooperative NOMA systems in terms of downtime probability and bias rate. With a focus on secure communications, the security of NOMA networks was evaluated in [10], where internal and external eavesdropping scenarios were carefully examined. Applying NOMA to random access, the author in [11] has shown that a Grant-free (GF) scheme based on NOMA can support huge connectivity by considering latency and reliability. To improve the spectrum utilization of an Unmanned Aerial

*Corresponding author. Email: tranquyhuu@iuh.edu.vn

Vehicle (UAV), the authors of [12] investigated the performance of coverage probability and achievable rate for NOMA communications with support UAVs. In [13], the authors introduced the use of NOMA for satellite networks and evaluated ground-based user outage behaviors with ordinal statistics. Or more recently, NOMA networks supporting backscatter communication have been studied in [14], which are capable of effectively supporting extremely large machine type scenarios.

Recently, with the advent of Reconfigurable Intelligent Surfaces (RIS) [15], systems with a combination of NOMA networks and RIS reconfigurable smart surfaces have been introduced. proposed and show that these two important technologies are very compatible and complement each other.RIS has proven to be one of the key technologies to achieve a smart radio environment (SRE) for the system's sixth generation (6G) network technology. wireless communication [16]. RIS can collect the wireless signal from the transmitter and beam it towards the receiver. In terms of composition, RIS is a surface consisting of N Metasurface (MS) elements (reflecting units), each of which is a reconfigurable reflector, that is, it can adjust the transmission medium to increase the transmit and receive capacity of wireless communication [17].

Specifically, RIS consists of quasi-passive reflectors, programmable and controlled via the RIS controller, which allows it to reflect and direct obstructed signals in desired directions. To make it necessary to adjust the phase shift of the reflecting elements to control the common phase of all scattering elements, the reflected phases and the angle of the incident Radio Frequency (RF) signal can be customized to produce the desired multipath effect. Reflected RF signals can be added to improve received signal power or suppressed to minimize interference [17].

From the advantages, such as low cost, it is a passive device. Without the aid of amplifiers, it can generate a beam to any desired direction and most importantly, easy operation. The ultra-thin surface makes RIS flexible in deployment and expansion [18]. Therefore, many related works on RIS have been proposed. Related works on RIS: Wireless communication with RIS support has attracted a lot of attention [19-21]. In [22], the authors investigated the channel performance of the RIS-powered network by RIS-illuminated spatial classification. With the goal of maximizing energy efficiency, the authors of [23] introduced low complexity approaches by jointly designing both the transmit power distribution and the phase shift of the reflecting elements. In [24], a statistical description of outage probability, error rate, and symbol error rate was outlined for RIS-enabled wireless communication over Rayleigh fading channels. In the Nakagami-m channel condition, the authors of [25] analyzed the performance of coverage probability for RIS-enabled communications systems by exploiting moment generators. To elucidate the impact of Line-of-Sight (LoS), the authors in [26, 27] evaluated the outage probability, ergodic capacity, and average symbol error probability of wireless operations with RIS support on Rician fuzzy channels. Except for the above contributions, several application scenarios, i.e., applying RIS to large device-to-device communications and facilitating simultaneous power and wireless transmissions have been highlighted. in [28]. Bidirectional communication between users supported by RIS was investigated in [29], where compatible or incompatible channels were calculated.

Based on the combination of two protocols RIS-NOMA is also interested and selected in the systems. Recent studies such as a system to serve users with NOMA by designing passive beamforming weights at RISs have been proposed in [30]. The results of the analysis demonstrate that the base station (BS) and user associations have little effect on the diversity orders achieved when the number of RIS is high enough. Calculation results are provided to confirm that the high Signal-to-Noise-Ratio (SNR) gradient of the RIS-supported network is one and that the proposed RIS-supported NOMA network has superior network performance compared to its orthogonal counterpart. Another wireless communication IoT model is introduced that exploits the main benefits of NOMA and RIS technologies in Simultaneous Wireless Information and Power Transfer (SWIPT) network which has been proposed in [31] The results highlight the benefits of public exploitation. RIS technology in the SWIPT IoT network supports NOMA and future direction. Another system, Simultaneously Transmitting And Reflecting Reconfigurable Intelligent Surface Non-Orthogonal Multiple Access (STAR-RIS-NOMA) proposed in [32], demonstrates that: 1) STAR-RIS-NOMA outage probability is better than that of STAR-RIS-supported Orthogonal Multiple Access (OMA) and conventional cooperative communication systems; 2) With the increase of K configurable factors and Rician factor κ, the STAR-RIS-NOMA network is capable of achieving performance enhancement; and 3) The ergodic rate of STAR-RIS-NOMA is higher than that of STAR-RIS-OMA.

The key contributions of this work are summarized as follows:

- First, we introduce the method of moments for characterizing the end-to-end channel (e2e) of a wireless system. In the Nakagami-m fading environment, we show that the distribution of the e2e channel coefficient magnitude of the system can be approximately equal to the Gamma distribution.
- Next, for system performance analysis, approximate closed-form expressions for the Outage Probability (OP) and Ergodic Capacity (EC) of the system are built. In addition, we provide specific analyzes on the accuracy of the proposed approximation distribution, i.e., accuracy in using the Gamma distribution to estimate the true distribution of the e2e channel coefficient.
- Finally, in our simulation, we consider the actual simulation settings, as shown in Table 1. Notably, our simulation results are in good agreement with the analysis formulas. included in all articles. From the above results, they reveal that the system using RIS support has a better direct path than the two systems: the system using RIS supporting no direct path and the system using no RIS in terms of OP and EC. In addition, our system achieves the highest Energy Efficiency (EE)

within a specific range of the target Spectral Efficiency (SE). We also built a simulation result of the actual RIS installation location. This result only shows that the number of elements installed at the RIS and the location of the RIS has a significant impact on system performance. In summary, we show that our proposed system is the most optimal in all three important parameters OP, EC and EE compared with the remaining models, as well as the impact of RIS placement. actual and the number of passive reflectors on the RIS to the system performance.

Notations. $\Gamma(.)$ denotes the Gamma function [[35]- eq. (8.310/1)], $\gamma(.,.)$ denotes the lower incomplete Gamma function [[35]- eq. (8.350/1)], $K_v(.)$ denotes the modified Bessel function of the second kind [[35]- eq. (8.407/1)], $X \overset{Approx.}{\sim} T(.)$ means X approximately follows the distribution $T(.)$. For parameters of distributions, η_X means the parameter η in the distribution of random variable X, $\omega_X(k)$ denotes the k-th moment of X, $E[X]$ denotes the expectation of X and ω_X the corresponding expected value, $[h]_r$ representing the element r-th of the vector h.

2. System model

We consider a low complexity communication system. There, the system has a Source (S) and a User (Destination) (D), both of which are equipped with a single- antenna node. (S) communicates with (D) via direct link supported by a Reconfigurable Intelligent Surface (RIS), R, which passively reflects signals from (S) to (D). The system is described as follows (**figure 1)**:

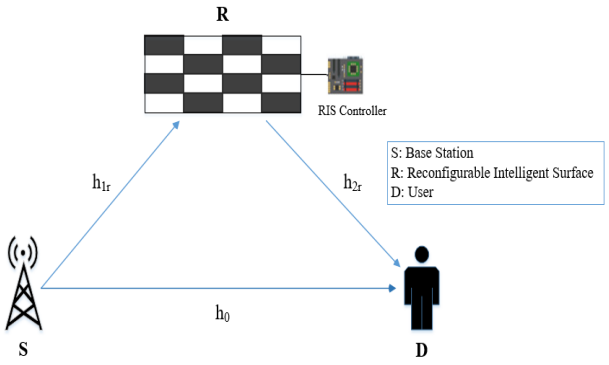

Figure 1. System model.

Assuming that a RIS (N=1) has L discrete reflector elements, we set $h_0 \in C$, $h_{1r} \in C^{L\times 1}$ and $h_{2r} \in C^{1\times L}$ to be the complex channel coefficient vectors from (S) to (D), from (S) to the second reflector RIS (R) and from this reflector element of RIS (R) to (D), respectively. The properties of RIS are characterized by a phase- shift matrix $\Psi = \kappa_r diag(e^{j\varphi_1},...,e^{j\varphi_L})$, where $\varphi_r \in [0,2\pi)$, $r = 1,...,L$, is the phase transition occurring at the element of the RIS and $\kappa_r \in (0,1]$ is the fixed amplitude of the reflector coefficient [45]; Knowing that, for a complex number z, we can represent $z = n(\cos\varphi + j\sin\varphi) = ne^{j\varphi}$ with $\varphi = \angle z, n = |z|$ and $|ne^{j\varphi}| = |ne^{-j\varphi}|, \forall n \in$, the channel poles can be represented as follows: $h_{cr} = h_{cr}e^{j\theta_{cr}}$ where $cr \in \{0,1r,2r\}, \theta_{cr} \in [0,2\pi)$. Let S is the transmit symbol at (S), with $E[|s|^2]=1$ normalized mean power expression, p_s be the transmit power of (S) [dBm], α be the additive white Gauss noise at the Destination (D) with zero mean and variance σ^2, i.e., $\alpha \sim CN(0,\sigma^2)$.

3. Performance analysis

3.1. Signal-to-noise ratio (SNR)

Definition: The signal-to-noise ratio, S/R, or SNR (Signal to Noise Ratio) is defined as the ratio between the output power of the transmitted signal and the power of the noise that damages that signal. This amplitude is measured, like almost everything related to sound and is expressed in decibel (dB) [38].

First, the signal that can be received at (D) is shown as follows:

$$y = (h_0 + \sum_{r=1}^{L} \kappa_r h_{1r} e^{j\varphi_r} h_{2r})\sqrt{p_s}s + \alpha \quad (1)$$

The end-to-end SNR (e2e) received at (D) is given by:

$$\rho = \bar{\rho}\left|e^{j\theta_0}\right|^2 \left|h_0 + \sum_{r=1}^{L} \kappa_r h_{1r} e^{j\phi_r} h_{2r}\right|^2 \quad (2)$$

Where $\phi_r \sim \varphi_r + \theta_1 + \theta_2 - \theta_0$ is the phase error of the RIS's rth reflector and $\bar{\rho} = \frac{p_s}{\sigma^2}$ represents the transmitted mean SNR [dB].

Let X be a Random Variable (RV) following the Nakagami-m distribution with the fading parameter m, Ω having a Probability Density Function (PDF) and a Cumulative Distribution Function (CDF) given by [37]:

$$f_X(x,m,\Omega) = \frac{2m^m}{\Gamma(m)\Omega^m} x^{2m-1} e^{-\frac{m}{\Omega}x^2}, x > 0 \quad (3)$$

$$F_X(x,m,\Omega)=\frac{\gamma(m,\frac{m}{\Omega}x^2)}{\Gamma(m)},x>0 \quad (4)$$

Proof: See **Appendix A**.

Where m > 0 is the *shape* parameter and Ω > 0 is the *spread* parameter of distribution. We have $X \sim Nakagami(m,\Omega)$. Note that the parameter Ω denotes the mean squared value of X, $\Omega = E[X^2]$, which is equivalent to the mean channel gain (power). The magnitude distribution of each channel coefficient can be expressed as: $h_0 \sim Nakagami(m_0,\Omega_0), h_{1r} \sim Nakagami(m_{h_1},\Omega_{h_1}), h_{2r} \sim Nakagami(m_{h_2},\Omega_{h_2})$

Let Y be a RV that follows a Gamma Distribution, with parameters being η,μ. The PDF and CDF are given by [40]:

$$f_Y(y,\eta,\mu)=\frac{\mu^\eta}{\Gamma(\eta)}y^{\eta-1}e^{-\mu y},y\geq 0 \quad (5)$$

$$F_Y(y,\eta,\mu)=\frac{\gamma(\eta,\mu y)}{\Gamma(\eta)},y\geq 0 \quad (6)$$

Proof: See **Appendix B.**

where, η > 0 is the *shape* parameter and μ > 0 is the *scale* parameter of the distribution. We have $Y \sim Gamma(\eta,\mu)$.

Theorem 1:

To simplify the notations, in the analysis we set $R \sim \kappa_r h_{1r} h_{2r}, A_R \sim \sum_{r=1}^{L} R, D \sim h_0 + A_R$, where D is the magnitude of the e2e channel coefficients.

Since $h_0 \sim Nakagami(m_0,\Omega_0)$, the k-th moment of h_0, $\omega_{h_0}(k) \sim \mathrm{E}[h_0^k]$, with $\mathrm{E}[h_0^k]$ be the mean of distribution [[39]- *eq. (65)*], which can be written as follows:

$$\omega_{h_0}(k)=\frac{\Gamma(m_0+\frac{k}{2})}{\Gamma(m_0)}(\frac{\Omega_0}{m_0})^{\frac{k}{2}} \quad (7)$$

Now, we turn our attention to the k-th moment of R. The exact PDF function of R given by ([39]- *eq. (90)*):

$$f_R(z)=\frac{4\lambda_r^{m_{h_1}+m_{h_2}}}{\Gamma(m_{h_1})\Gamma(m_{h_2})}x^{m_{h_1}+m_{h_2}-1}K_{m_{h_2}-m_{h_1}}(2\lambda_r z) \quad (8)$$

In there, $\lambda_r=\sqrt{\frac{1}{\kappa^2}\frac{m_{h_1}}{\Omega_{h_1}}\frac{m_{h_2}}{\Omega_{h_2}}}$. The detailed derivation in (8) can be briefly presented as follows.

The purpose of this inference is not only to accurately represent the PDF function of R, but also to show that the magnitude of the synthesized channel of the individual dual-hop channel with respect to a single reflecting element of a RIS in the system follows the Generalized-K (K_G) distribution [41, 43]. Back, for a given r, $R=\kappa_r h_{1r} h_{2r}$, where R represents the passively reflectors as independent RVs and identically distributed, h_{1r}, h_{2r} conversely as independent random variables but undistributed RVs. On the other hand, we know that $f_{XY}(z)=\int_0^\infty \frac{1}{x} f_Y(\frac{z}{x}) f_X(x)dx$, so the PDF of R can be rewritten to:

$$f_R(z)=\frac{1}{\kappa_r}\int_0^\infty \frac{1}{x} f_{h_{1r}}(\frac{z}{\kappa_r x}) f_{h_{2r}}(x)dx \quad (9)$$

Besides, we already have $h_{1r} \sim Nakagami(m_{h_1},\Omega_{h_1}), h_{2r} \sim Nakagami(m_{h_2},\Omega_{h_2})$, so from (3) the PDF of R is written as:

$$f_R(z)=\frac{4}{\Gamma(m_{h_1})\Gamma(m_{h_2})}(\frac{m_{h_1}}{\kappa^2\Omega_{h_1}})^{m_{h_1}}(\frac{m_{h_2}}{\Omega_{h_2}})^{m_{h_2}}z^{2m_{h_1}-1} \times\int_0^\infty x^{2m_{h_2}-2m_{h_1}-1}e^{(-\frac{z^2}{\kappa_r^2}\frac{m_{h_1}}{\Omega_{h_1}}\frac{1}{x^2}-\frac{m_{h_2}}{\Omega_{h_2}}x^2)}dx \quad (10)$$

Proof: See **Appendix C**.

The exact PDF of R is written to **(8)**.

Therefore, we can conclude that R follow the K_G distribution with the shape parameters is m_{h_1}, m_{h_2}. Based on the exact PDF of R, we get the k-th moment of R, defined as $\omega_R(k) \sim \mathrm{E}[R^k]=\int_0^\infty z^k f_R(z)dz$. Similarly **(7)**, $\omega_R(k)$ can be rewritten as:

$$\omega_R(k)=\frac{\Gamma(m_{h_1}+\frac{k}{2})\Gamma(m_{h_2}+\frac{k}{2})}{\Gamma(m_{h_1})\Gamma(m_{h_2})}\lambda_r^{-k} \quad (11)$$

Based on the k-th moment of R obtained in (11), we set according to the Gamma distribution. Note that, for a given r, R are independent and identical distributions RVs. We have [40]:

$$R \overset{Approx.}{\sim} Gamma(\eta_R,\mu_R) \quad (12)$$

Where:

$$\eta_R=\frac{(\mathrm{E}[R])^2}{Var[R]}=\frac{[\omega_R(1)]^2}{\omega_R(2)-[\omega_R(1)]^2} \quad (13)$$

$$\mu_R = \frac{\mathrm{E}[R]}{\mathrm{Var}[R]} = \frac{\omega_R(1)}{\omega_R(2) - [\omega_R(1)]^2} \quad (14)$$

And $f_R(z;\eta_R,\mu_R)$ shown as in **(5)**. The analysis will be based on the approximate PDF of R.

Therefore, the approximate distribution of A_R is:

$$A_R \overset{approx.}{\sim} Gamma(L\eta_R,\mu_R) \quad (15)$$

Therefore, the approximate CDF and PDF of AR are given by:

$$F_{A_R}(z) \approx \frac{\gamma(L\eta_R,\mu_R z)}{\Gamma(L\eta_R)} \quad (16)$$

$$f_{A_R}(z) \approx f_{A_R}(z,L\eta_R,\mu_R) \quad (17)$$

where **(17)** is expressed as **(5)**.

Using the polynomial deployment [[41]-eq. (12)], the k-th moment of AR, i.e., $\omega_{A_R}(k) \triangleq \mathrm{E}[A_R^k]$ be written as:

$$\omega_{A_R}(k) = \sum_{k_1=0}^{k}\sum_{k_2=0}^{k_1}\cdots\sum_{k_{L-1}=0}^{k_{L-2}} \binom{k}{k_1}\binom{k_1}{k_2}\cdots\binom{k_{L-2}}{k_{L-1}} \times \omega_{R_1}(k-k_1)\omega_{R_2}(k_1-k_2)\ldots\omega_{R_L}(k_{L-1}) \quad (18)$$

3.2. Outage probability (OP)

Definition: The Outage Probability of the system is the probability that the e2e signal-to-noise ratio is less than a given threshold value [47].

We first construct the correct distribution of the main component of D, i.e., A_R according to gamma distribution, which is shown in **(15)**.

We then obtain the approximate closed-form expressions for PDF and CDF of D. Specifically, since h_0 and A_R are independent RV and $h_0, A_R \geq 0$. We have the SNR e2e received at (D), **(2)** can be rewritten as:

$$\rho = \bar{\rho}(h_0 + A_R)^2 = \bar{\rho} D^2 \quad (19)$$

The statistical characteristics of the e2e channel coefficient magnitude are presented in the following theorem.

Theorem 2:

The approximate closed- form expressions for CDF and PDF of D can be obtained as follows, respectively:

$$F_D(x) \approx \Theta(x) \triangleq \sum_{m=1}^{M}[F_{h_0}(\frac{m}{M}x) - F_{h_0}(\frac{m-1}{M}x)] \times F_{A_R}(\frac{M-m+1}{M}x) \quad (20)$$

$$f_D(x) \approx \Delta(x) \triangleq \sum_{m=1}^{M}[[\frac{m}{M} f_{h_0}(\frac{m}{M}x) - \frac{m-1}{M} f_{h_0}(\frac{m-1}{M}x)] \times F_{A_R}(\frac{M-m+1}{M}x)\frac{M-m+1}{M} \times (F_{h_0}(\frac{m}{M}x) - F_{h_0}(\frac{m-1}{M}x)) f_{A_R}(\frac{M-m+1}{M}x)] \quad (21)$$

where $f_{h_0}, F_{h_0}, F_{A_R}$ presented in **(3)**, **(4)** and **(16)**.

Proof: See **Appendix D**.

Based on **Theorem 2**, a closed- form approximation for **OP** can be written as:

$$OP = \Pr(R \leq R_{th}) = \Pr(\rho < \rho_{th}) \quad (22)$$

With. $\rho_{th} = 2^{R_{th}} - 1$

Based on **(19), (22)** can be rewritten as:

$$OP = \Pr(\bar{\rho} D^2 \leq \rho_{th}) = F_{D^2}(\frac{\rho_{th}}{\bar{\rho}}) = F_D(\sqrt{\frac{\rho_{th}}{\bar{\rho}}}) \approx \Theta(\sqrt{\frac{\rho_{th}}{\bar{\rho}}}) \quad (23)$$

with $\Theta(\sqrt{\frac{\rho_{th}}{\bar{\rho}}})$ be written similarly to **(20)**.

3.3. Ergodic capacity (EC)

Definition: A process is called Ergodic when the time average can be substituted for the system-wide average. This means that the channel changes fast enough in the transmission time and goes through all fading states. An Ergodic channel can support the maximum error-free transmission rate with 100% confidence according to the following belows [46]:

$$EC = \mathrm{E}[\log_2(1+\rho)] = \mathrm{E}[\log_2(1+\bar{\rho} D^2)] = \frac{1}{\ln 2}\int_0^{\infty}\frac{1}{z+1}[1 - F_D(\sqrt{\frac{z}{\bar{\rho}}})]dz \quad (24)$$

In there, E is the mean, ρ is the instantaneous value of the signal-to-noise ratio (SNR). In contrast to the Ergodic channel, the channel is said to be non-Ergodic when it does not change fast enough to pass through all the fading states during the communication period. This happens when the channel is slowed down by fading obstruction or persists for too long during shadowing. Ergodic capacity is obtained when instantaneous capacity is averaged at all time values.

3.4. Energy efficiency (EE)

3.4.1. Total power consumption of the system

Definition: The total power consumed to operate the system including the transmit power at the Source (S), as well as the static power of the hardware components involved [34]. From there, the total power consumption of the system supported by RIS is presented as follows:

$$P_{Total} = P_S + P_{\text{RIS}} + P_S + P_D \text{ [mW]} \quad (25)$$

Where, P_S, P_D, P_{RIS} is the static power of the hardware consumed at (S), (D) and RIS, respectively.

In case of a system without RIS, the total power consumed by the system only includes the participation of transmit power at (S), hardware static power at (S) and (D). So we have:

$$P_{Total} = P_S + P_S + P_D \text{ [mW]} \quad (26)$$

3.4.2. Energy Efficiency (EE)

Definition: Energy efficiency is defined as the ratio between the system achievable sum rate and the total power consumption of the system [23].

From the above definition, the energy efficiency (EE) of the system is expressed as follows:

$$\text{EE} = BW \times \frac{R_{th}}{P_{Total}} \text{ [Mbit/Joule]} \quad (27)$$

where BW is the transmission bandwidth [MHz], P_{Total} is the total power consumption [mW] and R_{th} is the target SE [b/s/Hz] (with). BW P_{Total} R_{th} $R_{th} = \sum_{r=1}^{L} \log_2(1+\rho_{th})$

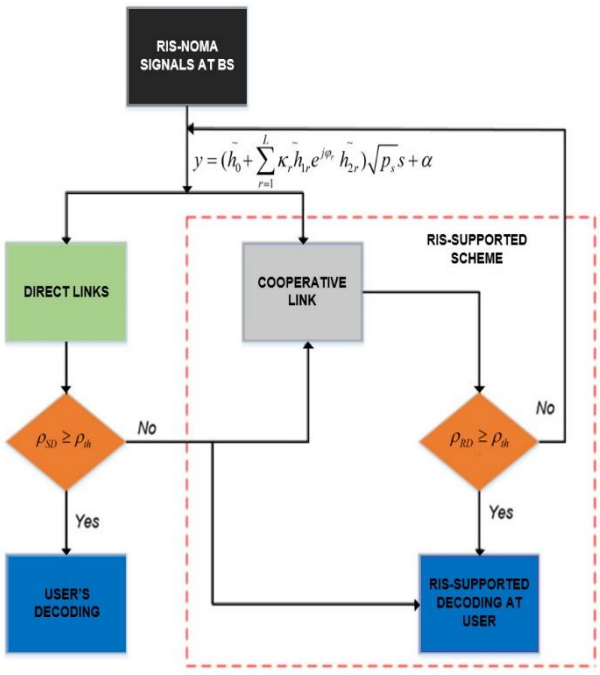

Figure 2. Illustration algorithm flowchart of the system

To clarify how the system works, we design a diagram as shown in **figure 2**. It shows that the signal from the source is decoded at the same time for both cases: decoding the information to the user by direct link and decoding of information to the user by cooperative forwarding using RIS. If the user fails to decode its own signal from the direct link in the first place, its received signal from the direct link is retained and combined with the cooperative relay signal via the use of RIS in second place. The decoded signal at the user is a combination of the two signals above.

IV. Numerical results

In this section, we provide the results on the PDF and CDF of D that follow the Gamma distribution, as well as the OP, EC of the system. The simulation results verify the correctness of the analytical formulas developed above and also to provide detailed information about the system's performance. The results indicate that changing the number of reflective elements of the RIS (L) and the location of the RIS affects the PDF and CDF and more importantly, it also affects the OP and EC parameters of the system. This is very important for the practical application of this surface, as well as being the foundation for developing this completely new technique to work more effectively in the future.

Table 1. Simulation parameters.

Parameters	Values	Parameters	Values
Bandwidth, BW	10 MHz [34]	Nakagami shape parameters, m	~ [2,3]
Carrier frequency, f_c	3 GHz [34]	Maximum elevation simulated position RIS, H(m)	10 m
Number of reflective elements, L	[50,75,100]	Noise power, σ^2	-94 dBm
S-D distance, d_{SD}	100 m	Coordinates set RIS [m]	x_R~ [5.95] and y_R~ [1,9]
Noise parameters, NF	10 dBm [34]	Transmission power, P_S [dBm]	[0,25]
The target SE, R_{th} [b/s/Hz]	1	Number of simulations	10^5
Thermal noise power density, N_0	-174 dBm/Hz [34]	Amplitude reflection coefficient, κ_r	1 [34]
Antenna gain, G_S, G_D [dB]	10 [34]	Static hardware power at (S), P_S and at (D), P_D [mW]	10 [23]
Static hardware power RIS, [mW] P_{RIS}	7.8 [23]		

Except for the other cases as below, the simulation parameters are set according to the values shown in Table 1. In which, the equivalent noise power at (D) is $\sigma^2 = N_0 + 10\log(BW) + NF$ [dBm]. Assuming non- Line of Sight (NLoS) condition in the 3GPP Urban Micro (Umi) pathloss model [36, 44], the attenuation path is integrated in the spread parameter of the Nakagami-m distribution $\Omega_{XY} = G_X + G_Y - 22.7 - 26\log(f_c) - 36.7\log(d_{XY}/d_0)$ [dB] [34], where dXY is the distance in the Descartes coordinates and d0 is the reference distance, here d0= 1 m. The number of M steps used in the M-staircase approximation is 100, M = 100. The simulated positions (S) and (D) are placed in the coordinate system of [0.0] and [100.0], respectively, the coordinates of the RIS are simulated at different coordinates are shown below:

4.1. Effect of the number of the RIS's reflecting elements (L) on system performance.

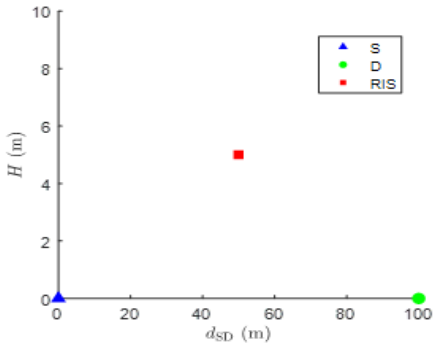

Figure 3. Coordinates of RIS in the case of xRIS= 50 and yRIS =5, [50.5].

Figure 3 describes the RIS position coordinates as x_{RIS}= 50 and y_{RIS} = 5 which are kept the same in all three cases comparing system performance using RIS-assisted RIS with direct link when changing the number of passive reflectors on the RIS is L=50, L=75 and L=100, respectively.

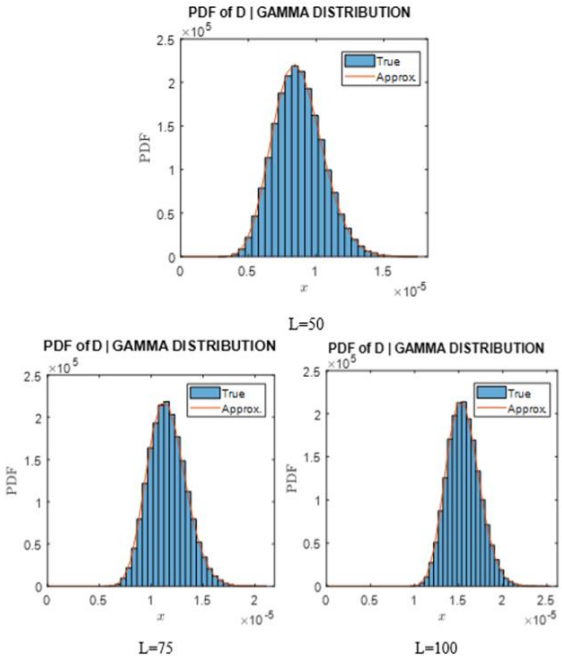

Figure 4. PDF of D in the following cases: L=50, L=75 and L=100.

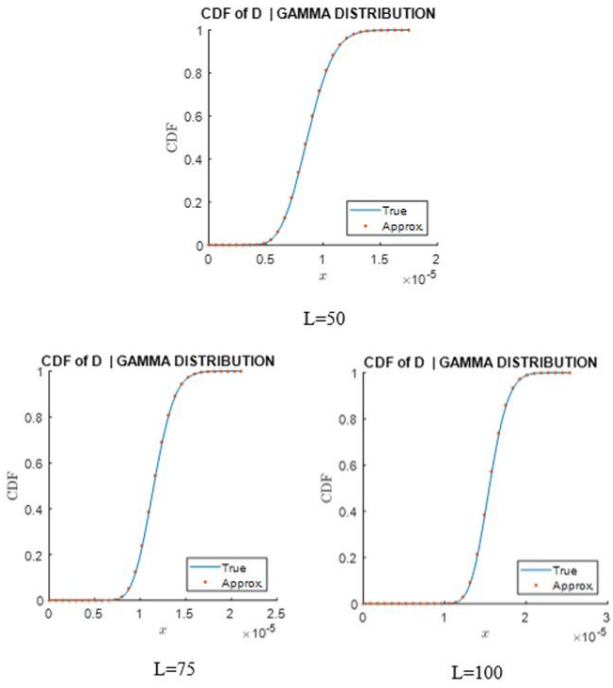

Figure 5. CDF of D in the following cases: L=50, L=75 and L=100.

Figures 4 and 5 describe approximate PDF and CDF that are well-suited to real PDF and CDF (**theorem 2**), which are numerically estimated based on data simulation. Besides, we also see that when we change the number of reflective elements (L), the variable range of x also changes, leading to changes in the variable values of PDF and CDF. Evidence, when increasing the number of RIS reflectors (L) from 50, 75 and 100, respectively, the x variability range also changes from 0.5 to 1.25, from 0.75 to 1.5 and from 1.25 to 2, respectively. And the x range changes, the value of the PDF and CDF also changes accordingly.

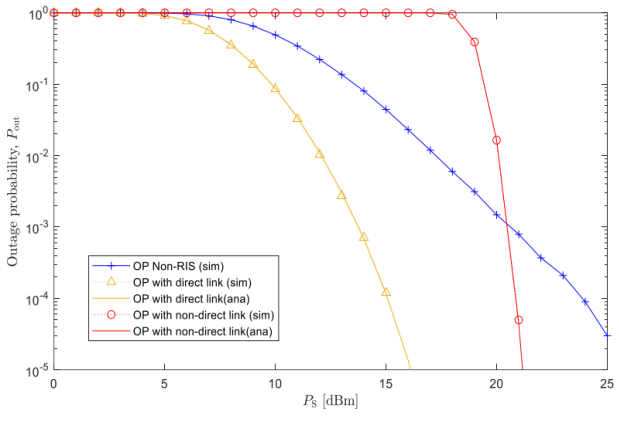

L= 50

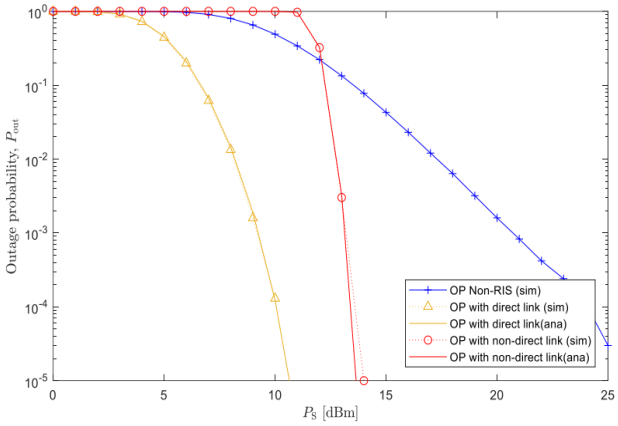

L= 75

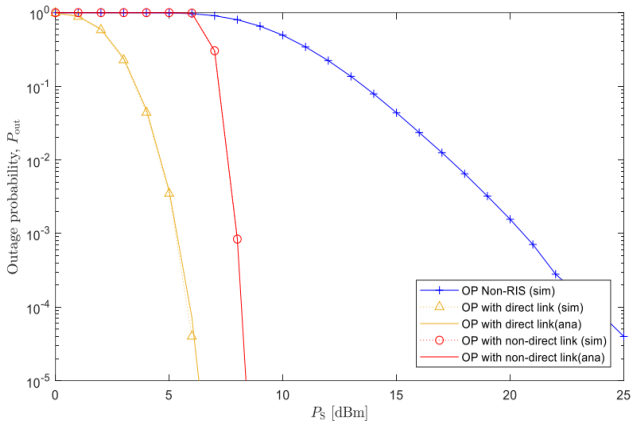

L= 100

Figure 6. Outage Probability (OP) in the following cases: L=50, L=75 and L=100.

Next, in **figure 6**, we have a simulation of the Outage Probability (OP) of the system with OP as a function of P_S, presented in Eq. **(23)**. As can be seen, the theoretical and simulated results are well corroborated, so our developed analytical formula is validated. In addition, we can see in **figure 6**, with fixed RIS coordinates, as the number of reflective elements (L) increases, the OP decreases sharply. The proof is that when we consider the case of the system using supported RIS with direct link, with L=50, when P_S = 10 dBm, OP equals 10^{-1}. With L=75, when P_S= 10 dBm, OP drops to less than 10^{-4}. With L=100, when the P_S = 10 dBm, the OP drops much deeper to less than 10^{-5}. In addition, the OP's simulation results also show that the system using supported RIS with direct link is the most optimal when compared with the other two systems: the system not using RIS and the system using supported RIS without direct link.

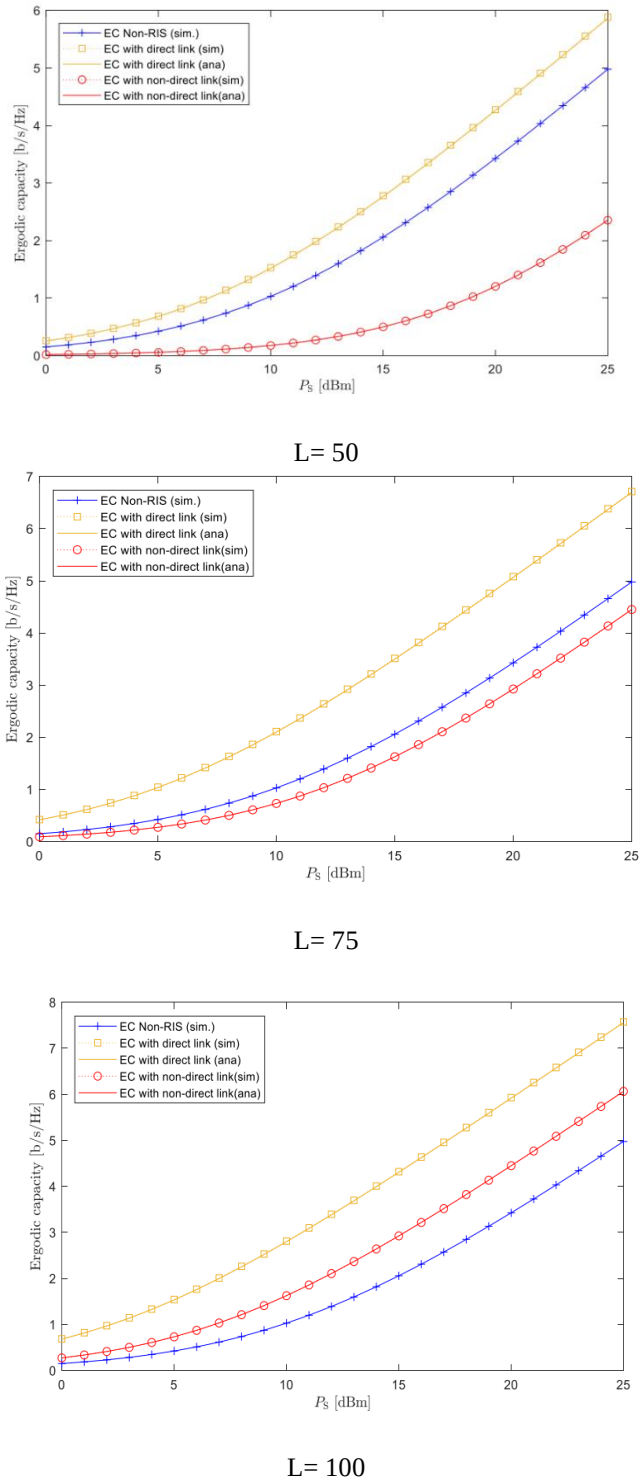

Figure 7. Ergodic capacity (EC) in the following cases: L=50, L=75 and L=100.

Similarly, in **figure 7**, we have a schematic diagram of the Ergodic capacity (EC) simulation of the system with EC as a function of P_S, presented in Eq. **(24)**. As can be seen, the theoretical and simulated results are well corroborated, so our developed analytical formula is validated. In addition, with a fixed RIS position (x_{RIS} = 50, y_{RIS} = 5), changing the number of reflective elements also changes the EC. For example, we consider the case of a system using supported RIS with direct link, with L =50, when P_S = 10 dBm, EC equals 1.5 [b/s/Hz]. With L = 75, when P_S = 10 dBm, EC increases to 2 [b/s/Hz]. With the RIS coordinate of [85;5], when P_S = 10 dBm, EC rises to almost 3 [b/s/Hz]. In addition, the simulation results of EC also show that the system using supported RIS with direct link is the most optimal when compared to the other two systems: the system not using RIS and the system using supported RIS without direct link.

4.2. Effect of RIS placement on system performance

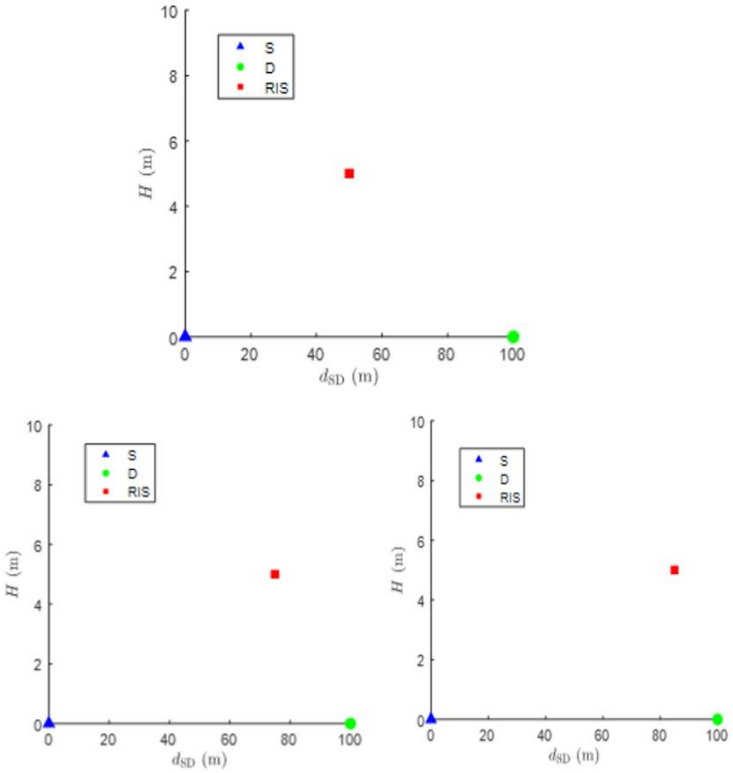

Figure 8. Coordinates of RIS in the following cases: [50.5], [75.5] and [85.5].

In this case, we set the coordinates of the RIS to [50.5], [75.5] and [85.5], respectively (**figure 8**) and keep the same number of reflectors (L) in all three cases as 50.

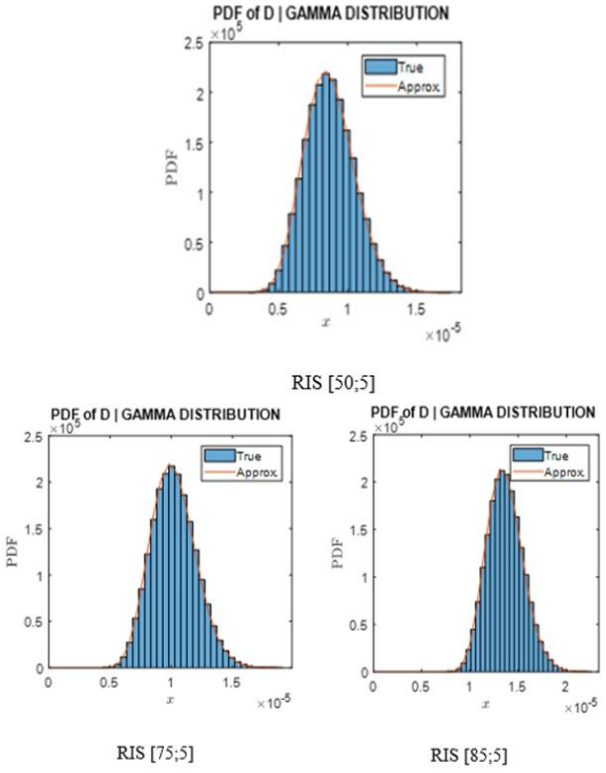

Figure 9. PDF of D in the cases of RIS coordinates is: [50.5], [75.5] and [85.5].

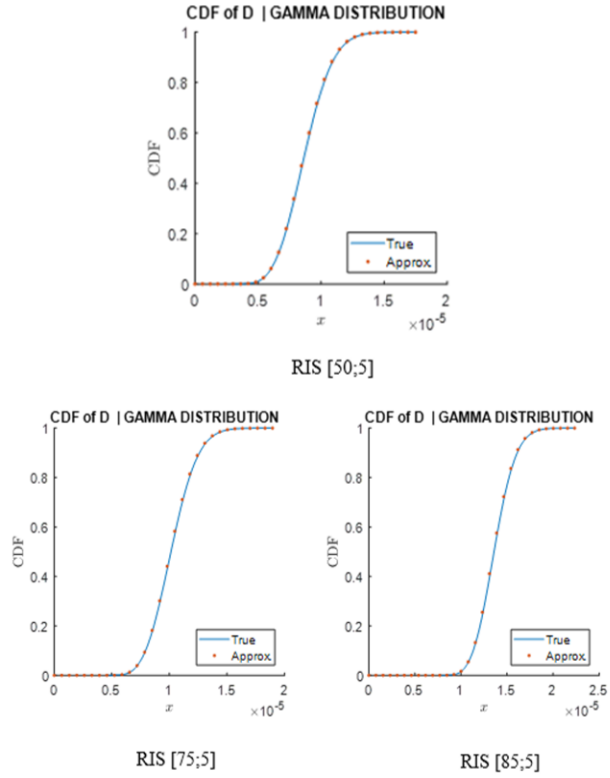

Figure 10. CDF of D in cases of RIS coordinates is: [50.5], [75.5] and [85.5].

Figures 9 and 10 describe approximate PDF and CDF that are well-suited to real PDF and CDF (**theorem 2**), which are numerically estimated based on simulated data. Besides, we also see that when we change the position of the RIS coordinates, the variable range of x also changes, leading to changes in the variable values of PDF and CDF. Evidence, when changing the RIS position from [50.5], [75.5] and [85.5], respectively. The variable range x also varies from 0.5 to 1.25, from 0.7 to 1.45 and from 1 to 1.75, respectively. And the x range changes, the value of the PDF and CDF also changes accordingly.

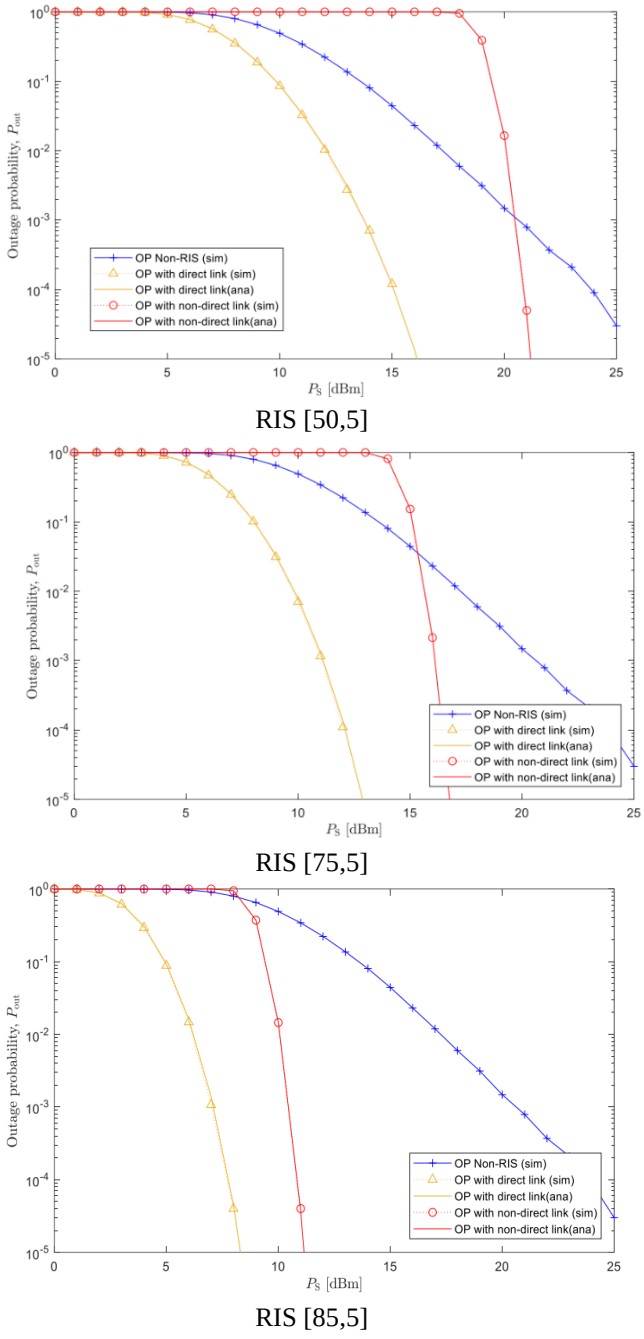

Figure 11. Outage Probability (OP) in cases of RIS coordinates is: [50.5], [75.5] and [85.5].

Next, in **figure 11**, we have a simulation of the Outage Probability (OP) of the system with OP as a function of P_S, presented in Eq. **(23)**. As can be seen, the theoretical and simulated results are well corroborated, so our developed analytical formula is validated. In addition, we can see in **figure 11**, with fixed RIS coordinates, with the number of reflectors (L) kept the same in three cases of 50, when the closer the RIS position (S) or (D), the more sharply the OP decreases. For example, we consider the case of a system using supported RIS with direct link, with RIS coordinates of [50;5], when P_S = 10 dBm, OP equals 10^{-1}. With a RIS coordinate of [75;5], when P_S = 10 dBm, OP drops to less than 10^{-2}. With a RIS coordinate of [85;5], when P_S = 10 dBm, OP drops to less than 10^{-5}. In addition, the OP's simulation results also show that the system using supported RIS with direct link is the most optimal when compared with the other two systems: the system not using RIS and the system using supported RIS without direct link.

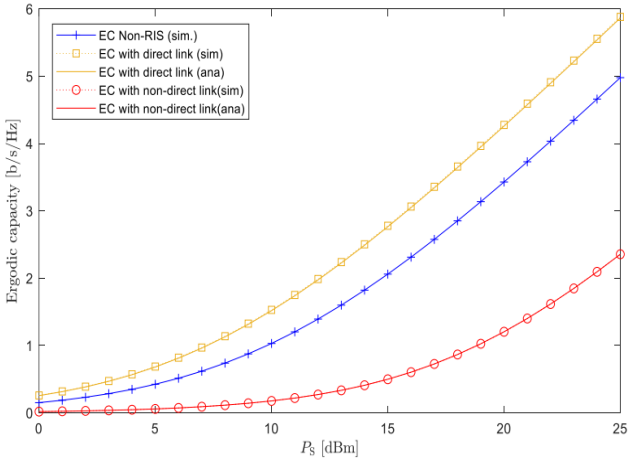

RIS [50,5]

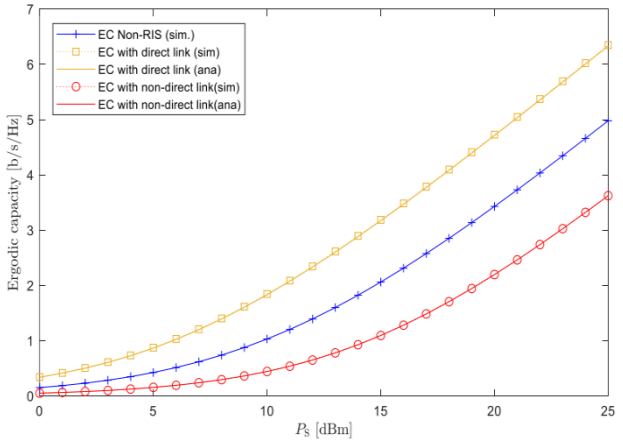

RIS [75,5]

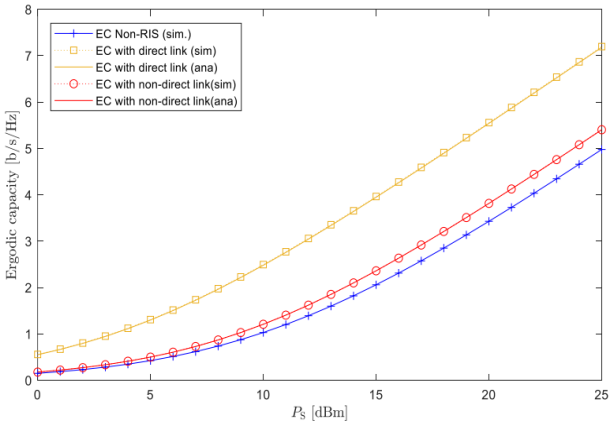

RIS [85,5]

Figure 12. Ergodic Capacity (EC) in the cases of RIS coordinates is: [50.5], [75.5] and [85.5].

Similarly, in **figure 12**, we have a schematic diagram of the Ergodic capacity (EC) simulation of the system with EC as a function of P_S, presented in Eq. **(24)**. As can be seen, the theoretical and simulated results are well corroborated, so our developed analytical formula is validated. In addition, with the number of elements (L) kept the same (L=50), placing the RIS as close as possible (S) or (D) also changes the EC. For example, we consider the case of the system using supported RIS with direct link, with a RIS coordinate of [50;5], when P_S = 10 dBm, EC equals 1.5 [b/s/Hz]. With a RIS coordinate of [75;5], when P_S = 10 dBm, EC increases to 2 [b/s/Hz]. With a RIS coordinate of [85;5], when P_S = 10 dBm, EC rises to almost 3 [b/s/Hz]. In addition, the simulation results of EC also show that the system using supported RIS with direct link is the most optimal when compared to the other two systems: the system not using RIS and the system using supported RIS without direct link.

4.3. Comparison of Energy Efficiency (EE) between a system using supported RIS with direct link, a system using supported RIS without direct link and a system not using RIS

Next, we will investigate the effect of the target SE (Rth) on the source transmit power (P_S) and the Energy Efficiency of the system (EE). Furthermore, we also compare the above parameters for the cases where the system using supported RIS with direct link, the system using supported RIS without direct link and the system not using RIS.

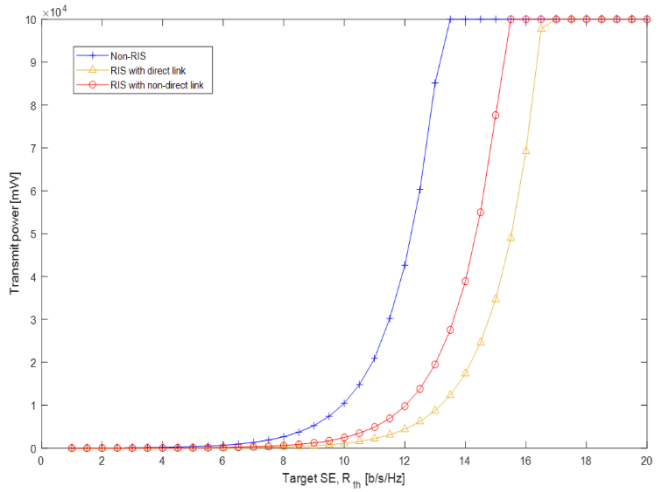

Figure 13. Comparison of the transmit power at (S), P_S [mW], between the system using supported RIS with direct link, the system using supported RIS without direct link and the system not using RIS, with P_S is a function of the target SE, Rth [b/s/Hz].

Figure 13 shows the simulation results of the transmit power (P_S) of the system, where P_S is a function of R_{th}. When R_{th} > 5.45 [b/s/Hz], the non- RIS system requires the highest transmit power, the RIS- supported direct link system requires the lowest transmit power. From that, we conclude that using supported RIS with direct link systems can help reduce the transmit power, leading to improved EE for the system. To prove the above conclusion, we will analyze the simulation results of EE in **Figure 14** below.

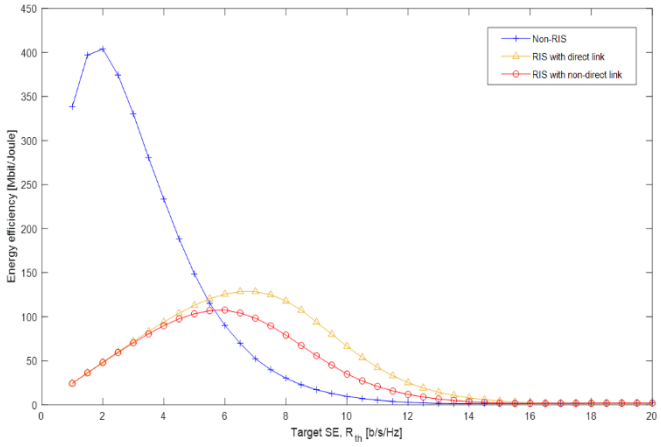

Figure 14. Comparison of Energy Efficiency, EE [Mbit/Joule], between the system using supported RIS with direct link, the system using supported RIS without direct link and the system not using RIS, with EE is a function of the target SE, Rth [b/s/Hz].

In **Figure 14**, we have a schematic diagram of EE simulation of the system with the EE as a function of R_{th}, presented in the Eq. **(27)**. Specifically, when $R_{th} \in$ (0; 5.45] [b/s/Hz], the system non using RIS provides the highest EE compared to the other two systems. Meanwhile, when R_{th} > 5.45 [b/s/Hz], the system using supported RIS with direct link provides the highest EE compared to the other two systems. Therefore, we can conclude that a system that transmits information directly from (S) to (D) is more appropriate both in terms of minimizing transmit power (P_S) and maximizing energy efficiency (EE), except when a high target SE (R_{th}) (greater than 5.45 b/s/Hz) is required, then we should use a supported RIS with direct link system to maximize system performance.

V. CONCLUSION

In this paper, we have studied a lowly complexity radio network model. Specifically, we used a relay network using a Reconfigurable Intelligent Surface (RIS) with a direct link. The Closed-form expressions of Outage Probability (OP) and Ergodic Capacity (EC) are considered. Based on the simulation of OP and EC, the results indicate that our proposed system is more optimal than the system using supported RIS without direct link and the system not using RIS. We have shown that given the total number of passive reflectors, the element allocation and location of the RIS have a significant effect on the performance of the system. Specifically, the more the number of reflectors and the closer the RIS is to the source or destination, the more it will help optimize the system. The analytical expressions match the simulation results through the Monte Carlo simulation method. Furthermore, the system using supported RIS with direct link achieves better EE than the other two systems when the value of the target SE reaches a specific value (more than 5.45 b/s/Hz). Therefore, the system using supported RIS with direct link will help reduce the transmit power and optimize the most energy compared to the other two systems.

Acknowledgement

The authors would like to thank the anonymous Reviewers for his/her efforts in spending time to process our paper.

Appendix

Appendix A

Let $F(x)$ is the CDF of $f(x) = 2(\frac{m}{\Omega})^m \frac{1}{\Gamma(m)} x^{(2m-1)} e^{\frac{-m}{\Omega}x^2}$ **(3)** (PDF of Nakagami-m distribution)

We have:

$$F(x) = \int_0^x f(x)dx = \int_0^x 2(\frac{m}{\Omega})^m \frac{1}{\Gamma(m)} x^{(2m-1)} e^{\frac{-m}{\Omega}x^2} dx$$

Put $t = \frac{mx^2}{\Omega} => dt = \frac{2mx}{\Omega}$

Then $F(x)=\int_0^x \frac{2}{\Gamma(m)}(\frac{m}{\Omega})^{m-1+1}x^{2m-1+1}e^{-\frac{m}{\Omega}x^2}dx$

$$=\int_0^x \frac{2}{\Gamma(m)}(\frac{m}{\Omega})x(\frac{mx^2}{\Omega})^{m-1}e^{-\frac{m}{\Omega}x^2}dx$$

$$=\frac{1}{\Gamma(m)}\int_0^{\frac{mx^2}{\Omega}} t^{m-1}e^{-t}dt$$

$$=\frac{\gamma(m,\frac{m}{\Omega}x^2)}{m} \quad (4)$$

APPENDIX B

Let $F(y)$ is the CDF function of $f(y)=\frac{\mu^\eta}{\Gamma(\eta)}y^{\eta-1}e^{-\mu y}, y\geq 0,$ (5) (PDF of Gamma distribution)

We have:

$$F(y)=\int_0^y f(y)dy=\frac{\mu^\eta}{\Gamma(\eta)}y^{\eta-1}e^{-\mu y}dy$$

$$=\frac{\mu^\eta}{\Gamma(\eta)}\int_0^y y^{\eta-1}e^{-\mu y}dy$$

Put $t=\mu y => y=\frac{t}{\mu}$

$$F(y)=\frac{\mu^\eta}{\Gamma(\eta)}\int_{b.0}^{\mu y}(\frac{t}{\mu})^{\eta-1}e^{-\mu(\frac{t}{\mu})}d(\frac{t}{\mu})$$

$$=\frac{\mu^\eta}{\Gamma(\eta)}.\frac{1}{\mu^{\eta-1}}.\frac{1}{\mu}\int_0^{\mu y}t^{\eta-1}e^{-t}dt$$

$$=\frac{1}{\Gamma(\eta)}\int_0^{\mu y}t^{\eta-1}e^{-t}dt$$

$$=\frac{\gamma(\eta,\mu y)}{\Gamma(\eta)} \quad (6)$$

APPENDIX C

Let $T=\int_0^\infty x^{2m_{h_2}-2m_{h_1}-1}e^{(-\frac{z^2}{\kappa_r^2}\frac{m_{h_1}}{\Omega_{h_1}}\frac{1}{x^2}-\frac{m_{h_2}}{\Omega_{h_2}}x^2)}dx$

$$v=2m_{h_2}-2m_{h_1}, \beta=\frac{m_{h_2}}{\Omega_{h_2}},$$

Put

$$\gamma=\frac{z^2}{k_r^2}\frac{m_{h_1}}{\Omega_{h_1}}, \rho=2.$$

Using [[35]- eq. (3.478/4)],

We have: $\int_0^\infty x^{v-1}e^{(-\beta x^\rho-\gamma x^{-\rho})}dx=\frac{2}{\rho}(\frac{\gamma}{\beta})^{\frac{v}{2\rho}}K_{\frac{v}{\rho}}(2\sqrt{\beta\gamma})$

At that time,

$$T=\frac{2}{2}(\frac{z^2}{k_r^2}\frac{m_{h_1}}{\Omega_{h_1}}\frac{\Omega_{h_2}}{m_{h_2}})^{\frac{2m_{h_2}-2m_{h_1}}{2.2}}K_{\frac{2m_{h_2}-2m_{h_1}}{2}}(2\sqrt{\frac{z^2}{k_r^2}\frac{m_{h_1}}{\Omega_{h_1}}\frac{m_{h_2}}{\Omega_{h_2}}})$$

$$=(\frac{z^2}{k_r^2}\frac{m_{h_1}}{\Omega_{h_1}}\frac{\Omega_{h_2}}{m_{h_2}})^{\frac{m_{h_2}-m_{h_1}}{2}}K_{m_{h_2}-m_{h_1}}(2z\sqrt{\frac{1}{k_r^2}\frac{m_{h_1}}{\Omega_{h_1}}\frac{m_{h_2}}{\Omega_{h_2}}})$$

Put, from $\lambda_r=\sqrt{\frac{1}{k_r^2}\frac{m_{h_1}}{\Omega_{h_1}}\frac{m_{h_2}}{\Omega_{h_2}}}$ (10) we have:

$$f_R(z)=\frac{4\lambda_r^{2m_{h_1}+2m_{h_2}}}{\Gamma(m_{h_1})\Gamma(m_{h_2})}z^{2m_{h_1}-1}\times(\frac{z^2}{k_r^2}\frac{m_{h_1}}{\Omega_{h_1}}\frac{\Omega_{h_2}}{m_{h_2}})^{\frac{m_{h_2}-m_{h_1}}{2}}K_{m_{h_2}-m_{h_1}}(2z\lambda_r)$$

$$=\frac{4\lambda_r^{2m_{h_1}+2m_{h_2}}}{\Gamma(m_{h_1})\Gamma(m_{h_2})}z^{2m_{h_1}-1}z^{2\frac{m_{h_2}-m_{h_1}}{2}}\times(\frac{1}{k_r^2}\frac{m_{h_1}}{\Omega_{h_1}}\frac{\Omega_{h_2}}{m_{h_2}})^{\frac{m_{h_2}-m_{h_1}}{2}}K_{m_{h_2}-m_{h_1}}(2z\lambda_r)$$

$$=\frac{4\lambda_r^{2m_{h_1}+2m_{h_2}}}{\Gamma(m_{h_1})\Gamma(m_{h_2})}z^{m_{h_1}+m_{h_2}-1}\times(\frac{1}{k_r^2}\frac{m_{h_1}}{\Omega_{h_1}})^{\frac{-m_{h_1}}{2}}(\frac{\Omega_{h_2}}{m_{h_2}})^{\frac{m_{h_2}}{2}}K_{m_{h_2}-m_{h_1}}(2z\lambda_r)$$

$$=\frac{4\lambda_r^{2m_{h_1}+2m_{h_2}}}{\Gamma(m_{h_1})\Gamma(m_{h_2})}z^{m_{h_1}+m_{h_2}-1}\times(\frac{1}{k_r^2}\frac{m_{h_1}}{\Omega_{h_1}})^{\frac{-m_{h_1}}{2}}(\frac{m_{h_2}}{\Omega_{h_2}})^{\frac{-m_{h_2}}{2}}K_{m_{h_2}-m_{h_1}}(2z\lambda_r)$$

$$=\frac{4\lambda_r^{2m_{h_1}+2m_{h_2}}\lambda_r^{2\frac{-m_{h_1}-m_{h_2}}{2}}}{\Gamma(m_{h_1})\Gamma(m_{h_2})}z^{m_{h_1}+m_{h_2}-1}\times K_{m_{h_2}-m_{h_1}}(2z\lambda_r)$$

$$=\frac{4\lambda_r^{2m_{h_1}+2m_{h_2}}\lambda_r^{-m_{h_1}-m_{h_2}}}{\Gamma(m_{h_1})\Gamma(m_{h_2})}z^{m_{h_1}+m_{h_2}-1}\times K_{m_{h_2}-m_{h_1}}(2z\lambda_r)$$

$$=\frac{4\lambda_r^{m_{h_1}+m_{h_2}}}{\Gamma(m_{h_1})\Gamma(m_{h_2})}z^{m_{h_1}+m_{h_2}-1}\times K_{m_{h_2}-m_{h_1}}(2z\lambda_r)$$

$$=(8)$$

We have proved Eq. (10) to (8).

APPENDIX D

First, we rely on the theorem of total probability [40] and the definition of conditional probability [40] to determine the probability of D. The CDF of D which can be given by:

$$F_D(x) = \Pr(D \le x) = \Pr((h_0 + A_R) \le x) \quad (28)$$

It can also be re-expressed as:

$$\begin{aligned} F_D(x) &= \Pr(\{A_R \le x - h_0\} \cap \{h_0 < x\}) \\ &= \int_0^x F_{A_R}(x-y) f_{h_0}(y) dy \end{aligned} \quad (29)$$

If we replace (16) in (29), it will lead to an integral analysis that is not expressed in closed- form. To solve this problem, (29) will be rewritten to:

$$F_D(x) = \int_0^x \int_0^{x-y} f_{A_R}(z) f_{h_0}(y) dz dy \quad (30)$$

Using the M-staircase approximation (*a method used to approximate the integral analysis of one or more layers, similar to the Riemann- Sum*[42]), (30) can be rewritten to:

$$F_D(x) \overset{M\to\infty}{\approx} \sum_{m=1}^{M} \int_{\frac{m-1}{M}x}^{\frac{m}{M}x} f_{h_0}(y) dy \int_0^{\frac{M-m+1}{M}x} f_{A_R}(z) dz \quad (31)$$

Integral analysis (31), we have:

$$\begin{aligned} F_D(x) &= \sum_{m=1}^{M} F_{h_0}(y) \Big|_{\frac{m-1}{M}x}^{\frac{m}{M}x} \times F_{A_R}(z) \Big|_0^{\frac{M-m+1}{M}x} \\ &= \sum_{m=1}^{M} [F_{h_0}(\frac{m}{M}x) - F_{h_0}(\frac{m-1}{M}x)] \times F_{A_R}(\frac{M-m+1}{M}x) \\ &= (20) \end{aligned}$$

Next, we take the derivative of (20), i.e., the PDF of D obtained as $f_D(x) = \frac{dF_D(x)}{dx}$ (21), in which the PDF, is given by A_R, $f_{A_R}(x)$ (17). The 2nd theorem has been proven.

References

[1] S. M. R. Islam, N. Avazov, O. A. Dobre and K. Kwak, Power-domain non- orthogonal multiple access (NOMA) in 5G systems: potentials and challenges, IEEE Communications Surveys & Tutorials, vol. 19, no. 2, pp. 721-742, (2017).

[2] S. Li, L. Bariah, S. Muhaidat, P. C. Sofotasios, J. Liang and A. Wang, SWIPT- enabled cooperative NOMA with mth best relay selection, IEEE Open Journal of the Communications Society, vol. 1, pp. 1798-1807, (2020).

[3] X. Wei, H. Al-Obiedollah, K Cumanan, M. Zhang, J. Tang, W. Wang and O. A. Dobre, Resource allocation technique for hybrid TDMA- NOMA system with opportunistic time assignment, IEEE International Conference on Communications Workshops (ICC Workshops), pp. 1-6, (2020).

[4] M. Zhang, K, Cumanan, W. Wang, A. G. Burr, Z. Ding, S. Lambortharan and O. A. Dobre, Energy efficiency optimization for secure transmission in a MIMO- NOMA system, IEEE Wireless Communications and Networking Conference (WCNC), pp. 1-6, (2020).

[5] Y. Yuan, Y. Wu, Z. Ding, X. You, H. V. Poor, and L. Hanzo, NOMA for next-generation massive IoT: Performance potential and technology directions, IEEE Commun. Mag., vol. 59, no. 7, pp. 115–121, (Jul. 2021).

[6] Y. Liu, W. Yi, Z. Ding, X. Liu, Dobre, Octavia, and N. Al-Dhahir, Application of NOMA in 6G networks: Future vision and research opportunities for next generation multiple access, (2021).
[Online] Available: https://arxiv.org/abs/2103.02334v1.

[7] Z. Ding, M. Peng, and H. V. Poor, "Cooperative non-orthogonal multiple access in 5G systems," IEEE Commun. Lett., vol. 19, no. 8, pp. 1462–1465, (Aug. 2015).

[8] Z. Zhang, Z. Ma, M. Xiao, Z. Ding, and P. Fan, Full-duplex device-to device-aided cooperative non- orthogonal multiple access, IEEE Trans. Veh. Technol., vol. 66, no. 5, pp. 4467–4471, (May 2017).

[9] X. Yue, Y. Liu, S. Kang, A. Nallanathan, and Z. Ding, Exploiting full/half-duplex user relaying in NOMA systems, IEEE Trans. Commun., vol. 66, no. 2, pp. 560–575, (Feb. 2018).

[10] X. Yue, Y. Liu, Y. Yao, X. Li, R. Liu, and A. Nallanathan, Secure communications in a unified non-orthogonal multiple access framework, IEEE Trans. Wireless Commun., vol. 19, no. 3, pp. 2163–2178, (Mar. 2020).

[11] R. Abbas, M. Shirvanimoghaddam, Y. Li, and B. Vucetic, "A novel analytical framework for massive grant-free NOMA," IEEE Trans. Commun., vol. 67, no. 3, pp. 2436–2449, (Mar. 2019).

[12] X. Li, Q. Wang, Y. Liu, T. A. Tsiftsis, Z. Ding, and A. Nallanathan, UAV-aided multi-way NOMA networks with residual hardware impairments, IEEE Wireless Commun. Lett., vol. 9, no. 9, pp. 1538–1542, (Sep. 2020).

[13] X. Yue, Y. Liu, Y. Yao, T. Li, X. Li, R. Liu, and A. Nallanathan, Outage behaviors of NOMA-based satellite network over shadowed rician fading channels, IEEE Trans. Veh. Technol., vol. 69, no. 6, pp. 6818–6821, (Jun. 2020).

[14] Z. Ding and H. Vincent Poor, "On the application of BAC-NOMA to 6G umMTC," IEEE Commun. Lett., vol. 25, no. 8, pp. 2678–2682, (Aug. 2021).

[15] Q. Wu and R. Zhang, Towards smart and reconfigurable environment: Intelligent reflecting surface aided wireless network, *IEEE Commun. Mag.*, vol. 58, no. 1, pp. 106-112, (Jan. 2020).

[16] M. Di Renzo, A. Zappone, M. Debbah, M.-S. Alouini, C. Yuen, J. de Rosny, and S. Tretyakov, Smart radio environments empowered by reconfigurable intelligent surfaces: How it works, state of research, and the road ahead, IEEE J. Sel. Areas Commun., vol. 38, no. 11, pp. 2450–2525, (Nov. 2020).

[17] E. Basar, M. Di Renzo, J. De Rosny, M. Debbah, M.-S. Alouini, and R. Zhang, Wireless communications through reconfigurable intelligent surfaces, IEEE Access, vol. 7, pp. 116753–116773, (2019).

[18] B. Di, H. Zhang, L. Song, and Z. Han, Reconfigurable Intelligent Surface for 6G: Communication, Sensing, and Localization, Tutorial Presentation at ICCC, (2020).

[19] S. Hu, F. Rusek, and O. Edfors, Beyond massive MIMO: The potential of data transmission with large intelligent surfaces, IEEE Transactions on Signal Processing, vol. 66, no. 10, pp. 2746–2758, (May 2018).

[20] L. Dai, B. Wang, M. Wang, X. Yang, J. Tan, S. Bi, S. Xu, F. Yang, Z. Chen, M. D. Renzo, C.-B. Chae, and L. Hanzo, Reconfigurable intelligent surface-based wireless communications: Antenna design, prototyping, and experimental results, IEEE Access, vol. 8, pp. 45 913– 45 923, (Mar. 2020).

[21] C. Pan, H. Ren, K. Wang, J. F. Kolb, M. Elkashlan, M. Chen, Y. Hao, J. Wang, A. L. S. Swindlehurst, X. You, and L. Hanzo, Reconfigurable intelligent surfaces for 6G systems: Principles, applications, and research directions, IEEE Commun. Mag., vol. 59, no. 6, pp. 14–20, (Jun. 2021).

[22] Y. Liu, X. Liu, X. Mu, T. Hou, J. Xu, M. Renzo, and N. Al-Dhahir, Reconfigurable intelligent surfaces: Principles and opportunities, IEEE Commun. Surveys Tutorials, vol. 23, no. 3, pp. 1546–1577, (May 2021).

[23] C. Huang, A. Zappone, G. C. Alexandropoulos, M. Debbah, and C. Yuen, Reconfigurable intelligent surfaces for energy efficiency in wireless communication, IEEE Trans. Wireless Commun., vol. 18, no. 8, pp. 4157–4170, (Jun. 2019).

[24] T. V. Chien, A. K. Papazafeiropoulos, L. T. Tu, R. Chopra, S. Chatzinotas, and B. Ottersten, Outage probability analysis of IRS-assisted systems under spatially correlated channels, IEEE Wireless Commun. Lett., vol. 10, no. 8, pp. 1815–1819, (Aug. 2021).

[25] H. Ibrahim, H. Tabassum, and U. T. Nguyen, Exact coverage analysis of intelligent reflecting surfaces with Nakagami-m channels, IEEE Trans. Veh. Technol., vol. 70, no. 1, pp. 1072–1076, (2021).

[26] Q. Tao, J. Wang, and C. Zhong, Performance analysis of intelligent reflecting surface aided communication systems, IEEE Commun. Lett., vol. 24, no. 11, pp. 2464–2468, (Nov. 2020).

[27] A. M. Salhab and M. H. Samuh, Accurate performance analysis of reconfigurable intelligent surfaces over Rician fading channels, IEEE Wireless Commun. Lett., vol. 10, no. 5, pp. 1051–1055, (May 2021).

[28] Q. Wu and R. Zhang, "Towards smart and reconfigurable environment: Intelligent reflecting surface aided wireless network," IEEE Commun. Mag., vol. 58, no. 1, pp. 106–112, (Jan. 2020).

[29] C. Pradhan, A. Li, L. Song, J. Li, B. Vucetic, and Y. Li, Reconfigurable intelligent surface (RIS)-enhanced two-way OFDM communications, IEEE Trans. Veh. Technol., vol. 69, no. 12, pp. 16 270–16 275, (Dec. 2020).

[30] T. Hou, Y. Liu, Z. Song, X. Sun, Y. Chen, and L. Hanzo, Reconfigurable Intelligent Surface Aided NOMA Networks, IEEE Commun. Lett., (Dec 2019).
[Online] Available: https://arxiv.org/abs/1912.10044 .

[31] M. Diamanti, E. E. Tsiropoulou and S. Papavassiliou, The Joint Power of NOMA and Reconfigurable Intelligent Surfaces in SWIPT Networks, IEEE Commun. Lett., pp. 621-625, (2021).
[Online] Available: https://arxiv.org/abs/10.1109/SPAWC51858.2021.9593111.

[32] X. Yue, J. Xie, Y. Liu, Z. Han, R. Liu and Z. Ding, Simultaneously Transmitting and Reflecting Reconfigurable Intelligent Surface Assisted NOMA Networks, IEEE Communications Letters , (2021).

[33] D. B. da Costa, H. Ding and J. Ge, Interference-limited relaying transmissions in dual-pop cooperative networks over Nakagami-m fading, IEEE Communications Letters, vol. 15, no. 5, pp. 503-505, (May 2011).

[34] E. Björnson, Ö. Özdogan and E. G. Larsson, Intelligent Reflecting Surface vs. Decode-and-Forward: How Large Surfaces Are Needed to Beat Relaying?, IEEE Communications Letters, vol. 9, no. 2, pp. 244-248, (Feb 2020).

[35] I.S.Gradshteyn and I.M.Ryzzhik, Table of Integrals, Series, and products, ed. 7, USA: Academic Press, New York, (2007).

[36] I. Yildirim, A. Uyrus and E. Basar, Modeling and Analysis of Reconfigurable Intelligent Surfaces for Indoor and Outdoor Applications in Future Wireless Networks, IEEE Communications Letters, (2020).

[37] Laurenson, D. I., Indoor Radio Channel Propagation Modeling by Ray Tracing Techniques, Edinburgh, Scotland, (1994).

[38] Mill, M., Signal-to-noise ratio or SNR in audio: What is it for?, 2021.
[Online] Available: https://itigic.com/vi/signal-to-noise-ratio-or-snr-in-audio-what-is-it-for/

[39] Nakagami, M., The m- Distribution- A general formula of intensity distribution of Rapid Fading, Faculty of Engineering, Kobe University, (1960).

[40] Peebles, P. Z., Probability, Random Variables and Random Signal Principles, ed. 4, USA: McGraw-Hill Science, New York, (2000).

[41] Petros S. Bithas, Nikos C. Sagias, P. Takis Mathiopoulos, George K. Karagiannidist and A. Rontogiannis, "Digital communications over Generalized- K fading channels", IEEE Communications Letters, pp. 684-687, (2005).

[42] Riemann, B., Riemann Sum, (1800s).
[Online] Available: https://en.wikipedia.org/wiki/Riemann_sum.

[43] S.Al- Ahmadi, H. Yanikomeroglu, "On the approximation of the Generalized- K distribution by a Gamma Distribution for modeling composite fading channels", IEEE Communications Letters, vol. 9.no. 2, pp. 706-713, (Feb 2010).

[44] S. Sun, T. S. Rappaport, S. Rangan, T. A. Thomas ,A. Ghosh, I. Z. Kovacs, I. Rodriguez, O. Koymen, A. Partyka and J. Jarvelainen, Propagation Path Loss Models for 5G Urban Microand Macro-Cellular Scenarios, IEEE Communications Letters, (2016).

[45] T. N. Do, G. Kaddoum, T. L. Nguyen, D. B. da Costa and Z. J. Haas, Aerial Reconfigurable Intelligent Surface-Aided Wireless Communication Systems, IEEE Communications Letters, (2021).

[46] Widanagamage, A., Ergodic Capacity and Outage Performance of Amplify-and-Forward Protocols, Queensland University of Technology, Brisbane, Queensland, Australia, (Mar 2013).

[47] V.T., Vo, Evaluation of multi-user random radio network performance on general fading channels, Post and Telecommunications Institute of Technology, Ho Chi Minh City, (2017).